Nano Energy 51 (2018) 639–648

Contents lists available at ScienceDirect

Nano Energy

journal homepage: www.elsevier.com/locate/nanoen

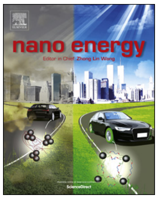

Full paper

N-doped C-encapsulated scale-like yolk-shell frame assembled by expanded planes few-layer $MoSe_2$ for enhanced performance in sodium-ion batteries

Hui Liu[a], Beihong Liu[a], Hong Guo[a,b,*], Mengfang Liang[a], Yuhao Zhang[a], Timur Borjigin[a], Xiaofei Yang[b], Lin Wang[a,*], Xueliang Sun[b,*]

[a] School of Chemical Science and Technology, School of Materials Science and Engineering, Yunnan University, No. 2, Green Lake North Road, Kunming 650091 China
[b] Nanomaterials and Energy Lab, Department of Mechanical and Materials Engineering, Western University, London, Ontario, Canada

ARTICLE INFO

Keywords:
Sodium ion batteries
Yolk-shell structure
N-doping few-layer $MoSe_2$
Rate performance

ABSTRACT

To meet the pressing needs of fast development of energy and environmental science, sodium ion batteries (SIBs) are considered as the promising novel generation of power storage system, due to abundant reserves and low price of sodium sources. In this work, N-doped C-encapsulated scale-like yolk-shell structured $MoSe_2$-C materials assembled by expanded (002) planes few-layer $MoSe_2$ nanosheets are successfully synthesized by a facile general strategy. The few-layer crystal fringes are no more than 4 layers. Notably, the interlayer spacing of (002) planes is expanded to 1.15 nm, which is larger than its intrinsic value of pristine $MoSe_2$ (0.64 nm). Particularly, the few-layer nanosheets with expanded (002) planes are spaced-restricted growing in the inner wall and the surface of hollow carbon frame and form scale-like yolk-shell hybrid $MoSe_2$-C structure. When evaluated as anode for SIBs, the $MoSe_2$-C materials show ultra-long cycling life, maintaining 378 $mA\,h\,g^{-1}$ over 1000 cycles at 3 $A\,g^{-1}$. It also exhibits outstanding rate capability and the Coulombic efficiencies for all the rate performance reaching more than 98.3% except the first one. The expanded (002) planes, 2D fewer-layer nanosheets and unique N-doped C-encapsulated scale-like yolk-shell frame are responsible for the enhanced electrochemical performance.

1. Introduction

Sodium-ion batteries have attracted great attention recently as the attractive alternative to Li-ion batteries due to abundant reserves and low price of sodium sources [1–3]. However, the large radius of Na ions (1.02 Å) compared with that of Li ions (0.76 Å) leads to many impacts. For example, graphite and silicon are electrochemical inactive for Na-ion batteries [4–6]. Meanwhile the anode materials for the SIBs still face severe challenges, such as low conductivity, large volume expansions, foot-dragging reaction dynamics, unsatisfied cycling time and inferior capacity and difficulty in seeking proper host materials for Na-ion storage [7–9]. Up to now, designing novel anodes with enhanced electrochemical performance including high reversible capacity, good rate capability, stable and long cycling life remains a major challenge unresolved, even though reports on cathodes of Na-ion battery have shown capability comparable to their Li-ion battery counterparts recently.

Two-dimension layered transition metal dichalcogenides (TMDs) have received considerable attention in the energy and environmental application field [10–13]. Particularly, MoS_2 has been extensively investigated as promising materials for LIBs and SIBs [9,14–17]. Chen et al fabricated hybrid MoS_2@C nanosheets, showing enhanced reversible capacity about 993 $mA\,h\,g^{-1}$ at 1 $A\,g^{-1}$ [18]. Nonetheless, it exhibits inferior cycling stability and low reversible capacities for SIBs. The short distance between neighboring layers of MoS_2 materials should be responsible for their poor electrochemical performance in SIBs. Furthermore, the MoS_2 nanosheets are easily to agglomerate together because of their high surface energy. Therefore, their practical application in SIBs is severely limited. It is noticed that $MoSe_2$ exhibits improved electrochemical performance for SIBs compared with MoS_2 due to its large pristine interlayer spacing (0.64 nm) and higher electrical conductivity due to little band gap, which is benefit to fast charge transfer and electrochemical cycling process [19–22].

To further increase the achieving performance $MoSe_2$ anodes, allowing the electrochemical reaction to proceed in a hybrid matrix of distinct material systems, such as coupling with electrically conductive carbon is a popular technology. Kang and coworkers prepared $MoSe_2$-rGO-CNT microsphere by a spray pyrolysis process, which exhibit final discharge capacities of 411 $mA\,h\,g^{-1}$ at 0.2 $A\,g^{-1}$ [23]. Unfortunately, the simple composite application of $MoSe_2$-C only improves their electrical conductivity, whereas the large volume change (ca. 300%) during charge/discharge process is difficult to buffer. Therefore, they

---

* Corresponding authors.
E-mail addresses: guohongcom@126.com (H. Guo), wangling@ynu.edu.cn (L. Wang), xsun9@uwo.ca (X. Sun).

https://doi.org/10.1016/j.nanoen.2018.07.021
Received 5 June 2018; Received in revised form 10 July 2018; Accepted 11 July 2018

normally deliver low rate capability.

The development of accurate designing molecular architecture of TMDs with functional nanostructures is another effective way to improve their electrochemical properties. Particularly, assembling 3D spatial structures with few layers 2D nanosheets has several advantages to overcome the shortcomings of bulk materials, because the single 2D nanosheets are easy to aggregate into large blocks during synthesis and electrochemical cycling process. Among them, yolk-shell structures attract great interest due to their unique structural features, fascinating physicochemical properties and widespread applications [24–28]. The core in the yolk-shell structures increase the energy density of SIBs through enhancing the weight ratio of the active contents. Meanwhile, the void part between the core and shell can effectively accommodate the severe volume variation of electrode materials upon cycling and prevent self-aggregation of the nanoscale subunits, which could alleviate the pulverization of active materials and significantly improve the cycling performance. The void structures can also facilitate electrolyte penetration and provide large contact area between the electrode and the electrolyte. Furthermore, it can short transport length for sodium ions and electrons, and thus improve the rate capability. Yu and coworkers prepared yolk-shell MoS_2 nanospheres used as anodes materials for lithium-ion battery, exhibiting long cycle life (94% of capacity retained after 200 cycles) and high rate behaviour (830 $mA\,h\,g^{-1}$ at 5 $A\,g^{-1}$) [29]. Whereas, the synthesis of yolk-shell structure is typically related to the template fabrication and multistep/high-cost procedures, which is easily to result the collapse of hollow structures. Thus, a novel controllable synthesis design for yolk-shell TMDs with high reversible capacity and long cycling life for SIBs is highly expected.

In most recently, it is interesting to notice that expanding the (002) planes of $MoSe_2$ can significantly improve the dynamics for sodium ion intercalating and deintercalating, and thus enhance sodium storage performance. Xu and coworkers prepared interlayer-expanded $MoSe_2$ nanosheets used as a highly durable electrode for sodium storage, exhibiting a reversible discharge capacity of 228 $mA\,h\,g^{-1}$ after 1500 cycles at a high current density of 1000 $mA\,g^{-1}$ [30]. However, most reports show unsatisfied capacities, particularly when the current density is higher than 2 $A\,g^{-1}$. Additionally, the nitrogen introducing defects within the carbon material can increase the electronic conductivity and create abundant active sites [31]. As compared to pure carbon, it is well documented that N-doping not only can tailor electronic structure and increase the chemical activity, but also benefit the contact between carbon and active materials [32].

Though these procedures are effective, each design strategy alone always leads to limited improvement on the electrochemical properties of TMDs for SIBs. Therefore, the development of a facile, scalable and controllable fabrication of durable hybrid yolk-shell structured TMDs materials with satisfactory cycling ability and high capacity is still highly desirable for SIBs. Herein, we design N-doped C-encapsulated scale-like yolk-shell frame $MoSe_2$-C assembled by few-layer $MoSe_2$ with expanded (002) planes to demonstrate our concept and propose a facile general strategy as illustrated in Scheme 1. The unique N-doped scale-like yolk-shell structures are benefit to the enhanced rate capability and long cycling life, The hollow multi-layer mesporous carbon sphere (HMLC) with ultrathin thickness acts as nanoreactors and can prohibit the restacking of $MoSe_2$, which is good to control the confined formation of few-layer $MoSe_2$ nanosheets with expanded interlayer spacing structure. Meanwhile the $MoSe_2$ nanosheets with expanded (002) planes are inclined to insert in HMLC matrix uniformly. As a result, the N-doped $MoSe_2$-C anode is rendered a higher reversible capacity, and the kinetics for sodium ion intercalating and deintercalating during electrochemical cycling are also improved as well.

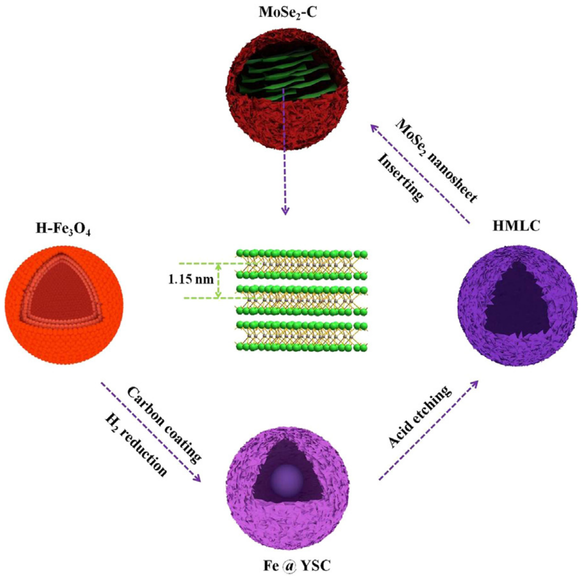

Scheme 1. Representative illustration of the assembly process of N-doped C-encapsulated scale-like yolk-shell structured $MoSe_2$-C.

2. Experimental section

2.1. Materials

$FeCl_3 \cdot 6H_2O$, sodium citrate, urea, polyacrylamide, tris, dopamine (PDA), hydrochloric acid solution (36–38%), Na_2MoO_4, ethylenediamine, selenium and hydrazine hydrate ($N_2H_4H_2O$, 80%) solution were all analytical grade and were used without further purification. Water used was purified using an Ulu-pure system (Shanghai China).

2.2. Synthesis of hollow Fe_3O_4 (H-Fe_3O_4) precursor

Typically, $FeCl_3 \cdot 6H_2O$ (1.08 g), sodium citrate (2.35 g), urea (0.72 g) were dissolved in 80 ml deionized water and stirred for 30 min to form a homogeneous solution. Then 0.8 g PAM (polyacrylamide) was added to the above solution with a continual stirring for 1.5 h. Subsequently, the above solution was transferred into a 100 ml Teflon-lined stainless steel autoclave and held at 200 °C for 12 h. Finally, the products were harvested through several rinse-centrifugation cycles with deionized water and absolute ethanol, then dried at 70 °C under vacuum condition overnight.

2.3. Synthesis of yolk-shell Fe@carbon (Fe@YSC)

The as-prepared H-Fe_3O_4 80 mg was dissolved in 100 ml 10 mM tris solution. Subsequently, 40 mg dopamine was added with magnetic stirring for 5 h to form the Fe_3O_4@PDA. Then, the Fe_3O_4@PDA was washed with ethanol and distilled water three times, and dried under vacuum at 60 °C overnight. Finally, the above product was sintered and reduced at 600 °C for 2 h under 20% H_2, 80% Ar atmosphere to turn into york-shell Fe@carbon (Fe@YSC).

2.4. Synthesis of hollow multi-layer mesporous carbon sphere (HMLC)

The Fe cores of Fe@YSC were removed by 4 M hydrochloric acid solution after 3 h of etching to prepare hollow multi-layer mesporous carbon sphere (HMLC).

2.5. Synthesis of $MoSe_2$-C

15.79 mg selenium was dissolved in 10 ml hydrazine hydrate solution stirring for 5 h. Then 24.2 mg Na_2MoO_4 was dispersed in 50 ml distilled water under constant stirring to form a clear solution. Subsequently, the above hydrazine hydrate-Se was added to Na_2MoO_4 solution slowly stirring for 30 min, followed by adding 5 ml ethylenediamine and dissolving 15 mg of HMLC into the solution. After ultrasonic dispersion for 1 h, the mixture was transferred to a 100 ml Teflon-lined autoclave and heated at 200 °C for needed time. The product was harvested by washed with deionized water and ethanol during rinse-centrifugation cycles before being dried at 60 °C in vacuum overnight. The characterization was shown in Supporting information.

2.6. Electrochemical measurements

For electrochemical performance evaluation, half-cell studies were performed. $MoSe_2$-C composites (80 wt%) was used as the working electrode with Super P carbon (10 wt%) and sodium alginate (10 wt%) in deionized water to form a uniform slurry which was then applied on copper foil and dried in vacuum at 80 °C for 48 h. The coin-type cells using CR2016 were fabricated with 1 M $NaClO_4$ in ethylene carbonate/diethyl carbonate (1:1 vol%) with 5 wt% fluoroethylene carbonate as the electrolyte, glass microfibers (Whatman) as separators and Na metal (Aladdin) as auxiliary electrodes. The coin cells are assembled in an argon-filled glove-box. The galvanostatic charge-discharge tests are at room temperature between 0.01 V and 3.0 V versus Na/Na^+ by a Land 2100 A tester. The cyclic voltammetry (CV) is performed on CHI660A electrochemical workstation between 0.01 and 3.0 V with scan rate of 0.05 mV s^{-1}

3. Results and discussion

3.1. Structure and morphology of scale-like yolk-shell $MoSe_2$-C frame

The synthesis strategy of scale-like yolk-shell $MoSe_2$-C structure assembled by interlayer-expanded few layer $MoSe_2$ nanosheets is illustrated in Scheme 1. The generative process of HMLC is shown in Fig. 1. Initially, H-Fe_3O_4 sphere assembled by little Fe_3O_4 nano particles with size about 2–5 nm is prepared as shown in scanning electron microscopy (SEM) and transmission electron microscopy (TEM) morphologies (Figs. 1a and b). The diameter of H-Fe_3O_4 is about 500 nm and the void part is the hollow structures can be observed obviously. Subsequently, Fe_3O_4@PDA formed by coating technology, and then it translates into N-doped scale-like yolk-shell structured Fe@YSC calcinated under H_2 to 600 °C with size about 500 nm uniformly as shown in Fig. 1c and d. It is interest that the little scatter Fe_3O_4 nano particles in the H-Fe_3O_4 precursor are reduced to Fe under H_2, and the Fe particles transfer and aggregate together into a large block, showing a distinguish yolk-shell structure. The X-ray diffraction analysis (XRD) results of H-Fe_3O_4 and Fe@YSC are shown in Fig. S1 (Supporting information), which is in agreement with SEM and TEM analysis. The X-ray photoelectron spectroscopy (XPS) spectra (Fig. S2 (Supporting information) of Fe@YSC samples exhibits that the N element exists in the product, reveling the Fe@YSC materials are doped by N which is resulted from PDA. Then the HCl is hired to remove the Fe and form HMLC as shown in Figs. 1e and f. The mesoporous is resulted from the mass transfer process in the formation of H-Fe_3O_4 and the reduction of Fe_3O_4. These pore canals are easy for the entrance of Mo, Se sources, which play the key role for the synthesis of $MoSe_2$-C product. Without the reduction of Fe_3O_4 and the remove of Fe, the few-layer $MoSe_2$ nanosheets cannot generate at all. Finally, the hollow carbon acts as nanoreactor, resulting in the confined formation of few-layer $MoSe_2$ nanosheets with expanded interlayer spacing. Meanwhile, ethylenediamine intercalating reagent also acts as a pivotal role to remote the formation of few-layer $MoSe_2$ nanosheets with expanded (002) crystal planes. Under hydrothermal system, some gases including NH_3 and CO_2 are produced in the reaction system by adding ethylenediamine (H_2N-CH_2-CH_2-NH_2). The rough porous carbon inner wall is an excellent condition for gas adsorption, resulting in a high concentration of these gases accumulating in the cavity of HMLC. As a result, the flaky $MoSe_2$ formed by the reaction of molybdenum source and the selenium source inserts in the inner wall and the surface hollow carbon frame due to the strong force of the gas. Because the flaky $MoSe_2$ is free to diffuse into the N-doped hollow carbon, the $MoSe_2$ nanosheets form and are confined in the carbon frame uniformly. Therefore, the hollow carbon nanoreactor plays a crucial role during this process, which not only provides the more active sites for generation of $MoSe_2$, but also promotes the confined growth of $MoSe_2$ in the internal carbon shell. Besides hollow carbon nanoreactor, ethylenediamine has another key role as an intercalating reagent to expand the interspacing of $MoSe_2$ layers. It can restrict the growth of $MoSe_2$ over certain molecular planes such as (002) plane. Furthermore, it controls the two-dimensional growth of $MoSe_2$ in hollow carbon shell frame to generate few-layer structures.

XRD patterns of the synthesized HMLC, scale-like yolk-shell $MoSe_2$-C and $MoSe_2$ reference are shown in Fig. 2a. The hollow carbon exhibits amorphous condition. The $MoSe_2$-C materials treatment is in good consistent with hexagonal $MoSe_2$ (JCPDS No. 29-0914). The molar ratio of Mo/Se in final products is nearly 0.51 according to quantitative chemical analysis by AAS HITACHI Z-2000, which value is matched with XRD results. The (002) planes of carbon peak at about 26.5° is indistinct owing to the $MoSe_2$ inserting into carbon layer uniformly, and the content of carbon is ca. 10.04 wt% as shown in the thermal gravity analysis (TGA) (Fig. S3 in SI). The patterns of reference pure $MoSe_2$ prepared without carbon exhibit extinct difference whether in peak position or intensity for the (002) diffraction peak. The relatively weaker (002) peak of the synthesized scale-like yolk-shell $MoSe_2$-C sample shows the confined growth over (002) crystal plane and multilayer stacking tendency of $MoSe_2$ is prohibited by the carbon layers, and thus form the fewer-layer structure. The interlayer distance of (002) plane of $MoSe_2$-C is expanded from 0.64 nm corresponding to pristine $MoSe_2$ to 1.12 nm by calculation according to Bragg equation. The remarkable prolonged value should be ascribed to the confined effect of ethylenediamine and carbon intercalating reagent. Furthermore, compared with pristine $MoSe_2$, the (002) crystal plane shifts from 13.2° to 11.8° distinguishedly, revealing its interlayer spacing of $MoSe_2$ layers expand significantly resulted from the carbonization. Therefore, the hollow mesoporous carbon layers and ethylenediamine act as crucial role in confined control effect for the formation of few-layer $MoSe_2$ nanosheets with expanded interspacing of (002) crystal plane.

The functional groups of the prepared $MoSe_2$-C and HMLC are shown in the fourier transform infrared spectroscopy (FTIR) spectrum (Fig. 2b). The peaks at ca.1617 and 1115 cm^{-1} of $MoSe_2$-C sample are resulted from C=O and C-O bonds of the organic solutions [33,34]. The broad absorption peaks centered at ca. 3419 cm^{-1} is associated with the asymmetric and symmetric stretching vibrations of the -OH group of absorbed water molecules. The inapparent peak at 1384 cm^{-1} is derived from C-N bond. The main peaks of $MoSe_2$-C product are almost the same as those peaks of HMLC, illuminating that the generated $MoSe_2$ few-layer nanosheets are distributed in the carbon layers uniformly and also are confined in the space of hollow carbon. Therefore, the FTIR spectrum doesn't detect different functional group characters, which result is in well lined with analysis of XRD patterns. The N_2 adsorption/desorption isotherms and the pore size distribution of the obtained $MoSe_2$-C sample are shown as Fig. S4 (SI), The isotherms are identified as type IV, which is the characteristic isotherm of mesoporous materials. The average pore diameter of $MoSe_2$-C and HMLC is about 3.952 nm and 3.993 nm, respectively, according to the pore size distribution data. The BET surface area of the sample 166.27 m^2 g^{-1} (Fig. S5 (SI)) is smaller than that of HMLC (1546.76 m^2 g^{-1}), which is good to the adsorption and thus can enhance the loading content of $MoSe_2$. The introduction of $MoSe_2$ nanosheets leads to the decrease of BET surface. The single-point total volume of pores at $P/P_0 = 0.155$ is 0.067 cm^3 g^{-1}, indicating the prepared samples have a loose mesoporous structure. The special hollow mesoporous architectures can

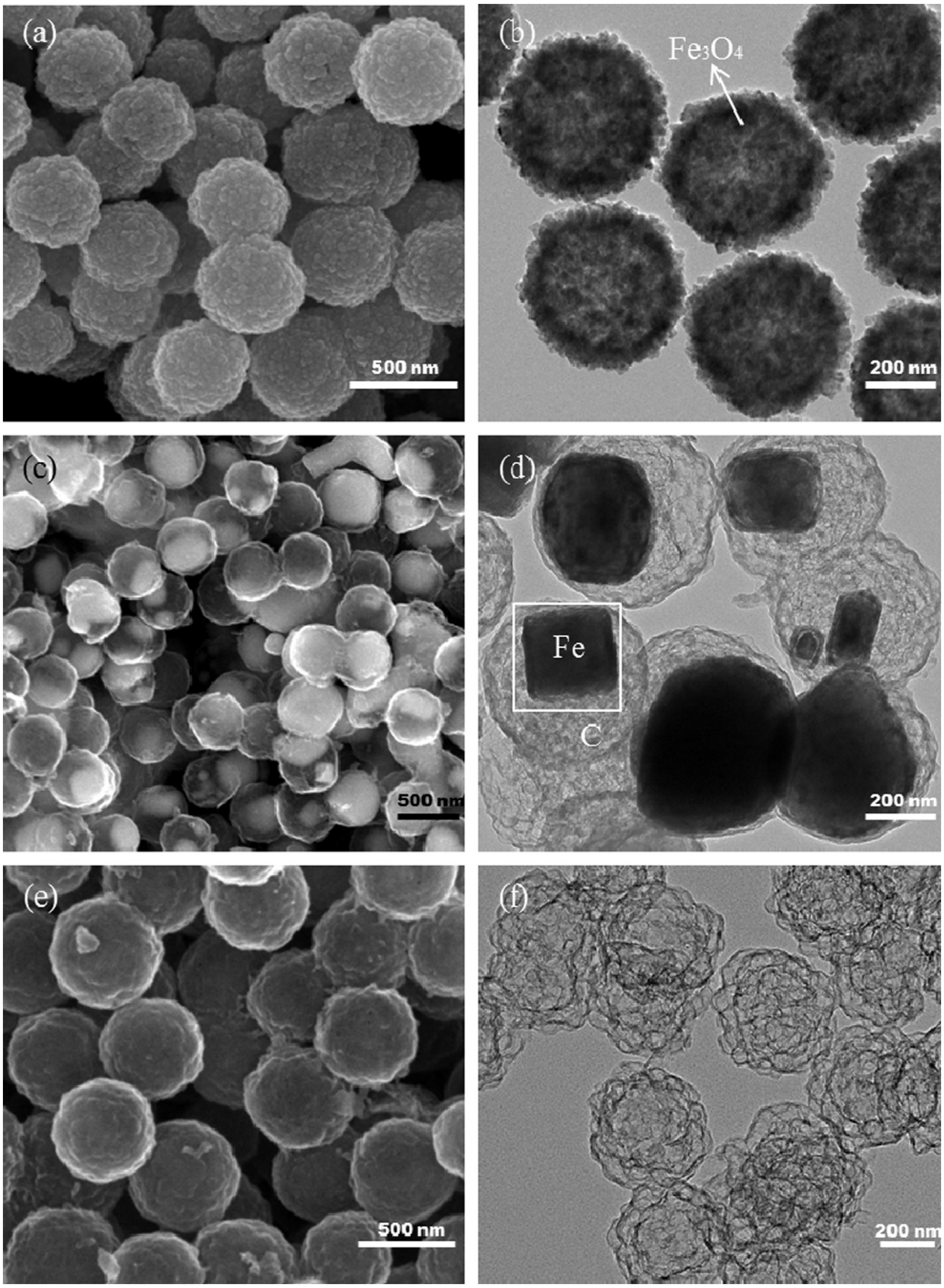

Fig. 1. SEM (a) and TEM (b) images of the prepared H-Fe_3O_4; SEM (c) and TEM (d) images of yolk-shell Fe@YSC reduced by H_2; SEM (e) and TEM (f) images of the fabricated HMLC.

accommodate the volume expansion during electrochemical reactions and thus avoid the pulverization of electrode. The Raman spectra are shown in Fig. 2c, exhibiting the strong Raman bands at 1369.92 cm^{-1} (D-band) and 1598.01 cm^{-1} (G-band) of $MoSe_2$-C respectively correspond to sp^3 hybrid and sp^2 hybrid of carbon atoms, respectively. These two peaks of carbon D and G band in $MoSe_2$-C are in good lined with HMLC, confirming the presence of carbon shell. Noticeably, the $MoSe_2$-C has two special Raman characteristic peaks due to the insertion of few-layer $MoSe_2$. The above two peaks attributed to the A_{1g} and E^1_{2g} modes of $MoSe_2$ Raman active are located at 239.18 and 286.24 cm^{-1}, which have an apparent red shift in comparation with the synthesized reference pure $MoSe_2$. The shift is dependent on the layer thickness to some extent according to other reports [23,37], suggesting the $MoSe_2$ layers restacking is prohibited in the prepared product. Therefore, the changed character of A_{1g} is resulted from signal averaging decided by average layer number of $MoSe_2$ nanosheets under the condition of laser interrogation spot. The subsequent TEM analysis can find further evidence to support these claims.

SEM and TEM images of the synthesized $MoSe_2$-C are shown in Fig. 3a–d, displaying the scale-like yolk-shell structured $MoSe_2$-C maintains the initial shape of HMLC. From the cracked particale in Fig. 3a, it can be noticed that the scale-like nanosheets are inserted in the carbon layers distinctly. This unique structure can increase the energy density of SIBs through enhancing the weight ratio of the active contents. The diameter of $MoSe_2$-C is about 500 nm and the average thickness of every layer in the hollow mesoporous hybrid system is about 2 nm according to Fig. 3b–d. The TEM images of the samples also exhibit the thin $MoSe_2$ nanosheets are confined growing in the inner wall and the surface of HMLC and combining with multi-layer carbon homogeneously without obvious aggregation, which is in good lined

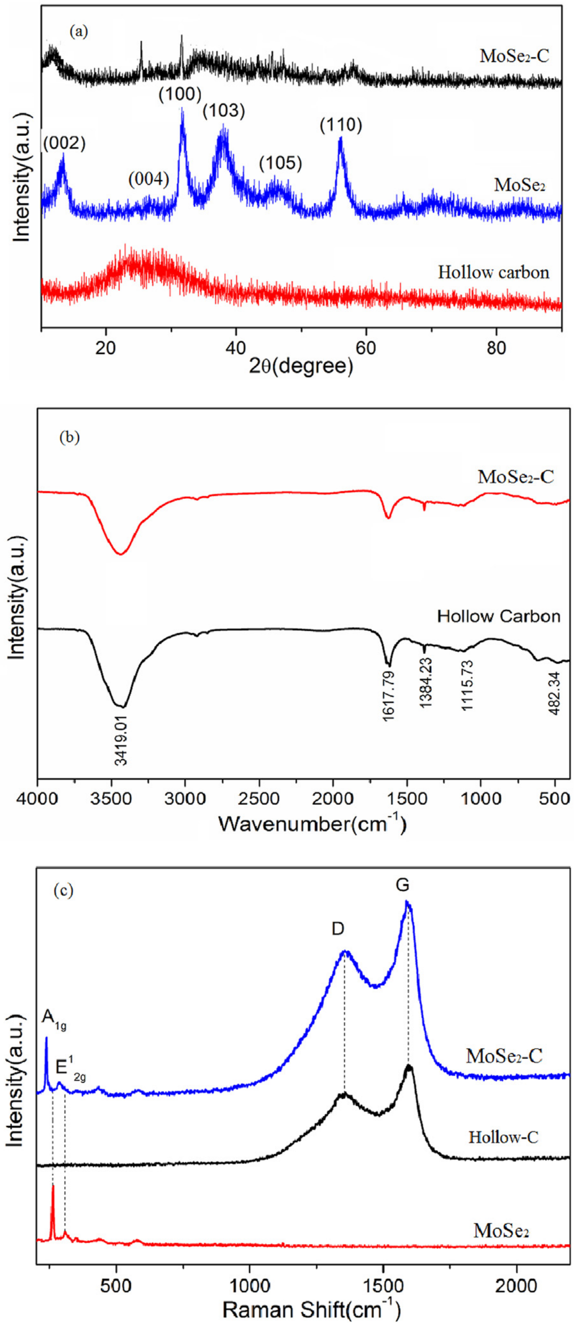

Fig. 2. XRD patterns (a), FTIR spectra (b) and Raman spectra (c) of $MoSe_2$-C, $MoSe_2$ reference and hollow carbon(HMLC).

with SEM and XRD analyses. The selected-area electron diffraction (SAED) patterns (Fig. 1e inset) reveal the diffraction rings 1–3 are indexed to (100), (103), and (110) diffraction of hexagonal $MoSe_2$ (JCPDS No. 29-0914). The $MoSe_2$-C composite is assembled by isolated thin sheets, while most of the current reports about $MoSe_2$ materials are stacked into aggregated blocks but not few-layer structures. It is remarkable to notice that this product shows the few-layer crystal fringes no more than 4 layers and even thin as few as 2 or 3 layers according to the high-resolution TEM (HR-TEM) image (Fig. 3e and f) distinctly. Therefore, the restriction and stabilization strategies of multi-layer carbon and the introducing of ethylenediamine play key roles to separate and prohibit the restacking of few-layer $MoSe_2$ nanosheets, and thus lead to the improvement of their cycling stability and rate capacities for SIBs. It is interesting that the interlayer spacing (002) plane of the $MoSe_2$ is expanded to 1.15 nm in zone A in Fig. 3e, which is far more than its intrinsic value of 0.64 nm. The unique effect of multi-layer mesoporous carbon can be responsible for the expanded (002) planes. Dramatically , in the zone B (Fig. 3f) the interplanar distance is expanded to as large as 1.72 nm, in which the increased value (0.57 nm) should be resulted from the sandwiched carbon since the value is smaller than the interlayer spacing. The elemental mapping images (Fig. 1g) ascertain the coexistence of N, Mo and Se is embedded in the hollow multi-layer carbon structure uniformly. Combined with the analysis of XRD, FTIR and Raman spectra, the expanded (002) planes few-layer $MoSe_2$ nanosheets are successful confined growing in the inner wall and the surface of HMLC uniformly and form scale-like yolk-shell structured hybrid $MoSe_2$-C composites.

Chemical compositions of the scale-like yolk-shell structured hybrid $MoSe_2$-C are further investigated by XPS analysis (Fig. 4). The survey spectra show the existence of C, Mo, Se and N elements (Fig. 4a). The N element is derived from the carbonization of PDA, revealing the prepared product is N-doped $MoSe_2$-C, which is benefit for the improvement of its conductivity and thus can enhance the rate capacity of $MoSe_2$-C anode. As seen from Fig. 4b, the peaks at 228.50 and 231.80 eV can be respectively attributed to 3d5/2 and 3d3/2 spin orbit peaks of the Mo 3d in the $MoSe_2$-C, suggesting the presence of the Mo IV state. The 3d peak of Se^{2-} (Fig. 4c) is split into well-defined 3d5/2 and 3d3/2 peaks at 54.34 and 54.76 eV. The C 1s peaks (Fig. 4d) at 284.66, 286.16, 287.30 and 288.56 eV are ascribed to C-C, C-O, N-sp^2 C and N-sp^3 C respectively. As shown in N 1s spectrum (Fig. 4e), the broad shoulder around 400 eV could be identified as three different nitrogen species, pyridinic-N at 398.2 eV, pyrrolic-N at 399.1 eV, and graphitic-N at 400.6 eV, suggesting the N is doped in the product sucessfully. These results are in agreement with other reports [30,33,35,36].

3.2. Electrochemical characterizations of $MoSe_2$-C

The electrochemical property of scale-like yolk-shell structured $MoSe_2$-C as anode for SIBs is researched by using CR2016 coin cells. The average active material mass loading in coin cells is average 3.12 mg/cm^2 and sodium plate acts as counter electrode. To investigate the effect of the scale-like yolk-shell structure vs. electrochemical properties of $MoSe_2$-C materials prepared with different time for the combination reaction of $MoSe_2$ and carbon from 2 to 24 h at 0.5 A g^{-1} are shown in Fig. 5a. It can be noticed that specific capacities remarkably increased with the increase of reaction time from 2 h to 24 h. The reversible capacity of $MoSe_2$-C corresponding to 24 h arrives at as high as 452.2 mA h g^{-1} after 500 cycles, which is far more than the value of 165.3, 378.5 and 386.7 mA h g^{-1} corresponding to the samples of 2, 6 and 12 h. Therefore, the $MoSe_2$-C product of 24 h is adopted as anode for the subsequent electrochemical test for SIBs.

The cyclic voltammetry (CV) tests are conducted at 0.05 mV s^{-1} and the curves for the first 3 cycles are shown in Fig. 5b, in which the apparent reduction peak at 0.58 V in the first cycle is assigned to the Na^+ inserting into the interlayer of $MoSe_2$ and forming Na_xMoSe_2 ($MoSe_2$ + xNa^+ + xe^- → Na_xMoSe_2) [19]. The reduction peak at 0.35 V is ascribed to the conversion reaction from Na_xMoSe_2 to Mo metal and Na_2Se with the formation of a solid electrolyte interphase (SEI) film (Na_xMoSe_2 + (4-x)Na^+ → $2Na_2Se$ + Mo^{4+}). These peaks disappear in the successive cycles. This is validated by ex situ XPS and HR-TEM measurements according to other previous researches [38,39]. The additional weak reduction peaks at 1.56 and 1.36 V are resulted from the redox of Mo nanoparticles [40,41]. The oxidation peak at 1.74 V is observed and which can be assigned to oxidation of Mo to $MoSe_2$ ($2Na_2Se$ + Mo^{4+} → $MoSe_2$ + $4Na^+$) [33]. The discharge-branch voltammogram for the initial cycle is substantially different from those of the following ones, revealing an irreversible transformation and structure rearrangement occurred. From the 2nd cycle, the CV curves almost overlap very well, demonstrating the good reversibility of the

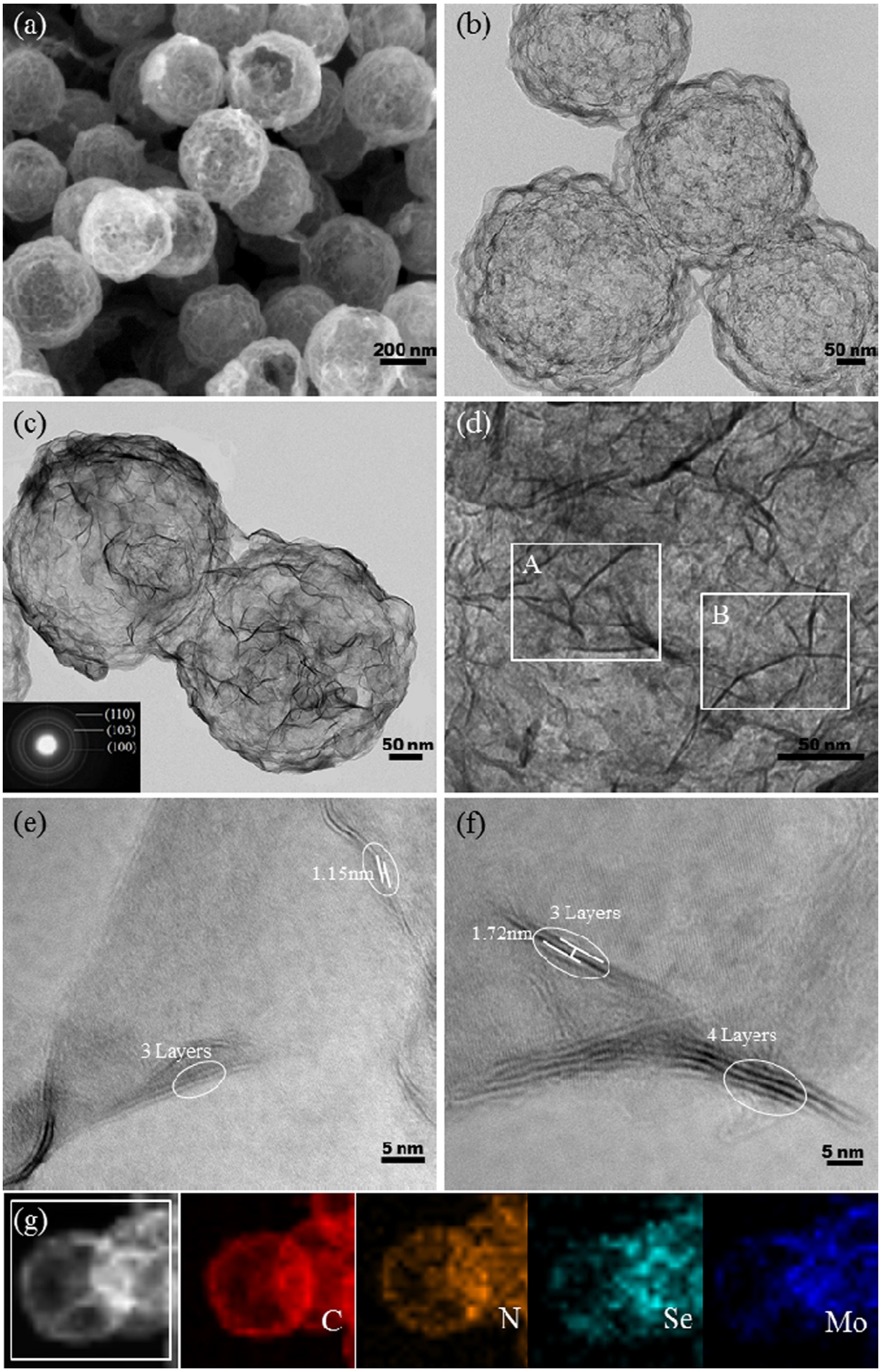

Fig. 3. SEM (a), TEM (b–d); SAED (inset in Fig. c) and HR-TEM images of the prepared $MoSe_2$-C (e–f); EDX mapping images (g, the element of C, N, Se, Mo) of the fabricated $MoSe_2$-C samples.

scale-like yolk-shell structured $MoSe_2$-C materials during cycling process.

The galvanostatic curves of sodium ion intercalation/deintercalation of $MoSe_2$-C anode at current of $0.5\,A\,g^{-1}$ are shown in Fig. 5c, which is in good consistent with CV profiles. According to the 1st, 2nd, and 100th discharge (Na^+ insertion) and charge (Na^+ extraction) curves, there is a wide, steady discharging plateau since 1.25 V in the first cycle, followed by a gradual voltage decrease. The initial discharge and charge capacities are 732.5 and $489.3\,mA\,h\,g^{-1}$, respectively. The initial capacity loss is $243.2\,mA\,h\,g^{-1}$, which should be attributed to the formation of solid electrolyte interphase (SEI) and the reduction of metal oxide to metal with Na_2Se formation [19–23,30,33]. These results are consistent with CV analysis. From the 2nd cycle, the long plateau was changed to a long slope from 2.0 to 0.05 V. The reversible capacity still maintained at $472.5\,mA\,h\,g^{-1}$ after 100 cycles, testifying the excellent electrode reversibility. Particularly, advantages of $MoSe_2$-

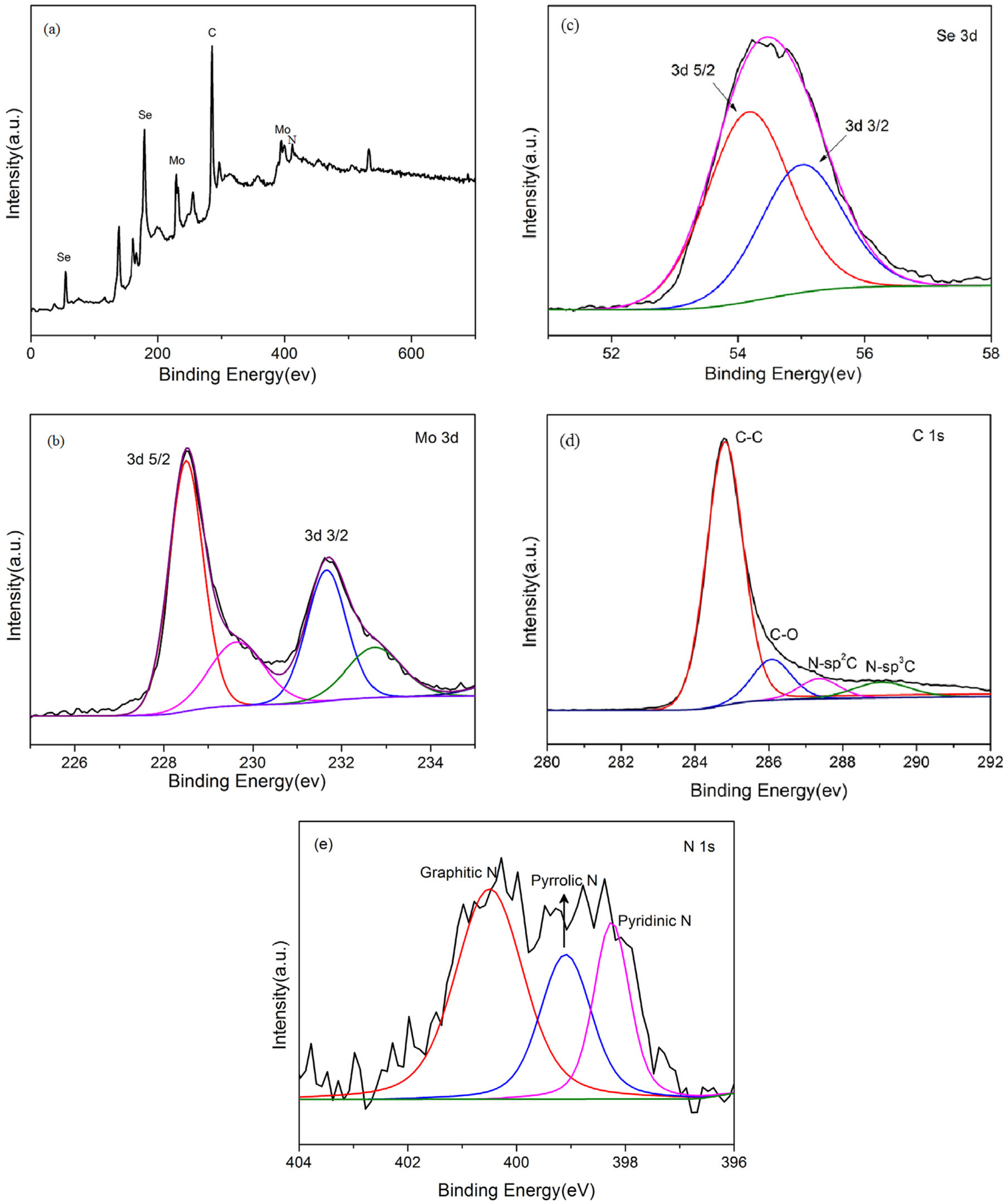

Fig. 4. XPS spectra of the as-prepared $MoSe_2$-C: (a) survey spectrum, (b) Mo 3d, (c) Se 3d spectrum, (d) C 1s and (e) N 1s spectrum.

C include a high rate capability, high capacity retention and low production costs.

Fig. 5d exhibits rate capacities of the $MoSe_2$-C at different currents from 1 A g^{-1} to 10 A g^{-1} for each 40 cycles. After 40 cycles at 1 A g^{-1}, the discharge capacity is 476.3 mA h g^{-1}. When the current increased to 3 A g^{-1}, its reversible capacity is also keep more than 442.5 mA h g^{-1} after 80 cycles. Even when the current rises to as high as 5 and 10 A g^{-1}, the capacity can also retain at 372.2 and 308.6 mA h g^{-1} respectively. Finally, the capacity recovers to 475.6 mA h g^{-1} when the current reduces to 1 A g^{-1} after 200 cycles. Particularly, all the different rates display stable during electrochemical cycling, demonstrating its superior reversibility. Notably, the $MoSe_2$-C materials exhibit ultra-long cycling life as shown in Fig. 5e, from which its discharge capacity remains 378.3 mA h g^{-1} over 1000 cycles at 3 A g^{-1}. Moreover, the Coulombic efficiencies reach more than 98.3% except the first one. These results show the prepared scale-like yolk-shell structured $MoSe_2$-C anode assembled by interlayer spacing expanded few-layer $MoSe_2$ nanosheets has a higher reversibility and robust stability. It is notable noticed that the capability and long-life cycling performance display significant enhancement compared with most other reports about anodes for SIBs elsewhere in recently, such as $CoSe_2$ @C@CNTs,[42] MoS_2,[43] MoS_2:C,[44] MoS_2/C [45] and NiS [46] in Table S1 (SP). The reversible capacity, rate capability, cycling stability and life of these materials are not competitive with this scale-like yolk-shell $MoSe_2$-C anode. Furthermore, to discover the good electrochemical stability is originated from its robust structure of scale-

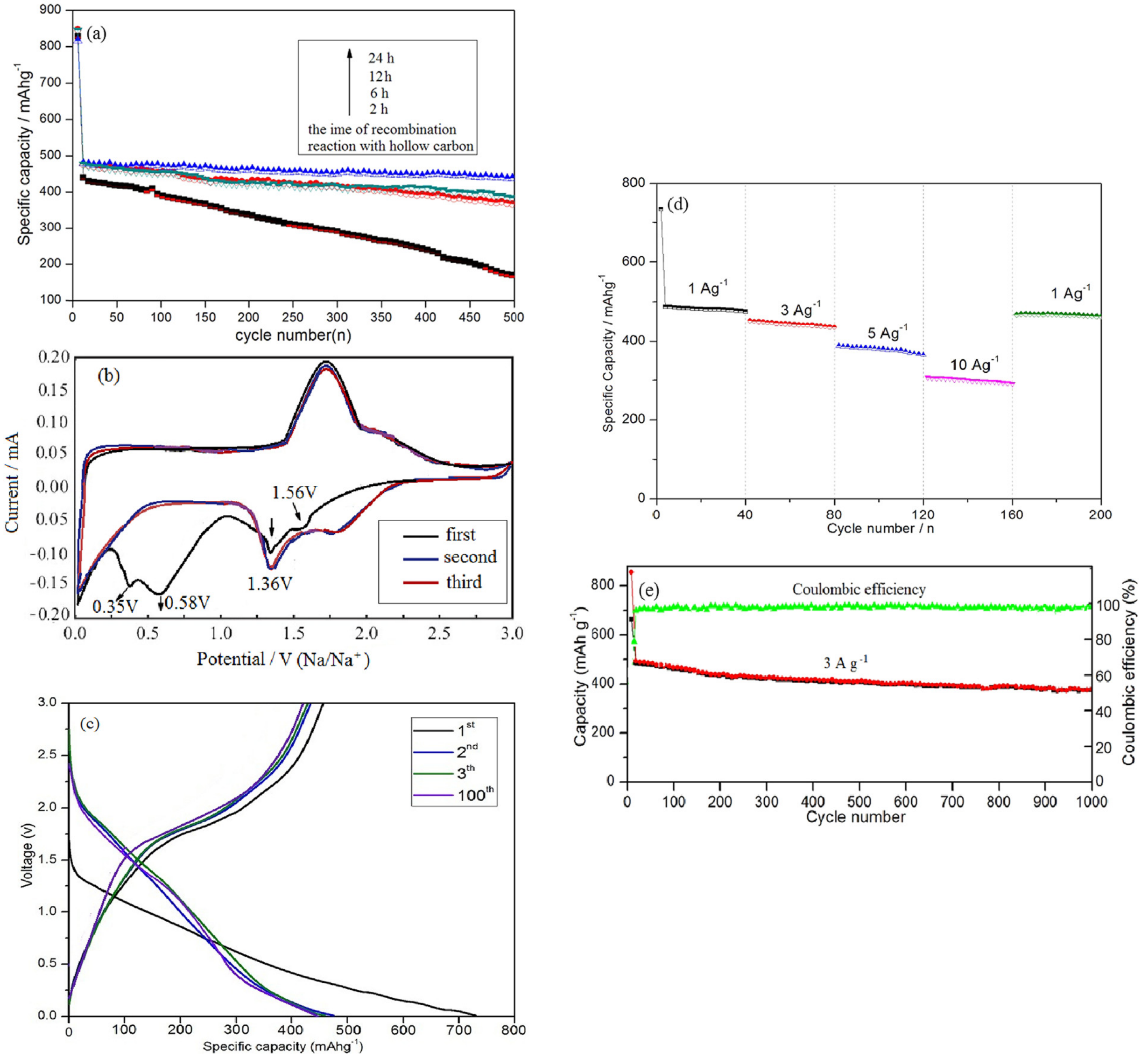

Fig. 5. Electrochemical performance of the prepared scale-like yolk-shell structured $MoSe_2$-C for SIBs (electrode potential range of 0.01–3.0 V vs. Na/Na^+): (a) Cycling performance with different times for the combined reaction between $MoSe_2$ and HMLC from 2 h to 24 h at a constant current density of 0.5 A g^{-1}. (b) CV curves with a scan rate of 0.05 mV s^{-1}. (c) Charge/discharge curves for the first 3 and the 100th cycles at current density of 0.5 A g^{-1}. (d) Rate capability of $MoSe_2$-C from 1 A g^{-1} to 10 A g^{-1}. (e) Cycling capability of $MoSe_2$-C with prolonged cycle life (1000 cycles) at 3 A g^{-1}.

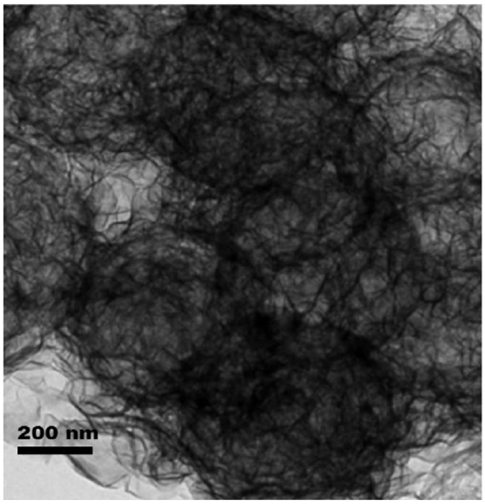

Fig. 6. TEM image of $MoSe_2$-C electrode after 1000 cycles at 3 A g^{-1}.

like yolk-shell structured $MoSe_2$-C anode, the TEM image is used to analysis the structure of sample after 1000 cycles at current density of 3 A g^{-1} as shown in Fig. 6. It is interest that the integrated frames of $MoSe_2$-C are also well held without breakage after 1000 cycles during Na^+ insertion/extraction.

In terms of the electrochemical impedance spectroscopy (EIS), as shown in Fig. 7, to analysis their reaction dynamics of $MoSe_2$-C and reference pristine $MoSe_2$ anode. The semicircle in medium frequency band is related to electrochemical reaction impedance, while the inclined line in low frequency zone is related to the solid-state ion diffusion in the electrode bulk. The diameter of semicircle corresponding to $MoSe_2$-C is obvious smaller than that of pristine $MoSe_2$ in fresh cell system, revealing the charge transfer efficiency of $MoSe_2$-C increased significantly. Meanwhile, the ionic conductivity is also improved because the slope of profile in low frequency corresponding to $MoSe_2$-C is larger than that of pure $MoSe_2$. In fact, the Ohmic resistance (Rs) of is simulated as 2.8 Ω, which is lower than that of pristine $MoSe_2$ (9.7 Ω). The calculated charge-transfer resistance (Rct) of $MoSe_2$-C is 105.2 Ω, which is also lower than that of pristine $MoSe_2$ (578.6 Ω). The smaller

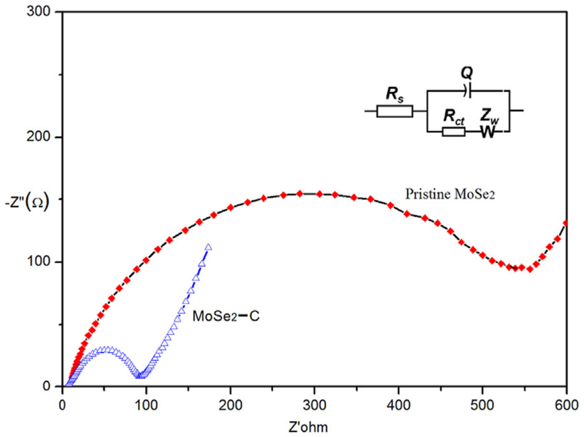

Fig. 7. EIS spectra of $MoSe_2$-C and $MoSe_2$ reference before cycling and the equivalent circuit (inset).

impedance of $MoSe_2$-C illuminates the enhanced charge transfer dynamics. The hollow multi-layer mesporous carbon structure, N-doping, and introducing of ethylenediamine play the key role in reaching enhanced Na^+ storage properties. The unique hollow confined carbon frame and embedded interlayer expanded few-layer $MoSe_2$ nanosheets exhibit significant advantages. The scale-like yolk-shell structures can shorten the length of Na^+ diffusion, which is benefit for the rate performance. The hollow structure offers a sufficient void space, which sufficiently alleviates the mechanical stress caused by volume change. The few-layer nanosheets enhance the permeation of electrolyte into the inner part of active materials, thus increase the contact zone. N-doping and C-encapsulation further increase the ionic and electronic conductivities of $MoSe_2$-C materials. Expanded interspacing of (002) crystal plane of $MoSe_2$ is benefit to the improvement of the dynamics for sodium ion intercalating and deintercalating during electrochemical reaction. Therefore, the $MoSe_2$-C electrode exhibits ultrahigh electrochemical performance.

4. Conclusions

In summary, few-layer $MoSe_2$ nanosheets with expanded (002) planes are successful confined growth in the inner wall and the surface of hollow multi-layer N-doped carbon and form mesoporous scale-like yolk-shell structures size about 500 nm. The $MoSe_2$ exhibits few-layer crystal fringes no more than 4 layers and the interlayer spacing is expanded to 1.15 nm. When applied as anodes for SIBs, the $MoSe_2$-C materials exhibit ultra-long cycling life with discharge capacity retaining 378 mA h g^{-1} over 1000 cycles at 3 A g^{-1}. Notably, the Coulombic efficiencies for all the rate performance reach more than 98.3% except the first one. Even when the current rise to as high as 10 A g^{-1}, the capacity can also retain at 308 mA h g^{-1}, and the capacity recovers to 475 mA h g^{-1} when the current reduces to 1 A g^{-1} after 200 cycles. Such superior untra-long cycling life and high rate capacity are attributed to their unique carbon stabilized scale-like yolk-shell $MoSe_2$-C hybrid frame, N-doping, expanded (002) crystal planes, and few-layer structure of $MoSe_2$ nanosheets, which improve the transfer efficiency of the electrons and ions, enhance the electrical conductivity, buffer the volume change and promote the reversible desodiation/sodiation of the $MoSe_2$-C anode. Therefore, the N-doped C-encapsulated scale-like yolk-shell $MoSe_2$-C anodes display great potential application for SIBs. This general strategy can also be worthy to further explore other advanced materials used in energy and environmental science.

Acknowledgements

H. L. and B. H. L. contributed equally to this work. The authors would like to acknowledge financial support provided by Major State Basic Research Development Program of China (973 Program, No. 2014CB643406), National Natural Science Foundation of China (No. 51474191 and No. 21467030), National Natural Science Foundation of China (No. 51474191 and No. 21467030), Key National Natural Science Foundation of Yunnan Province (No. 2018FA028), and the Program for Outstand Young Talents of Yunnan University (No. 201807).

Supporting information

Characterization, the XRD results of H-Fe_3O_4 and Fe@YSC (Fig. S1), the XPS spectra of Fe@YSC samples (Fig. S2), TG analysis of of as-prepared $MoSe_2$-C (Fig. S3), nitrogen adsorption/desorption isotherms of as-prepared $MoSe_2$-C (Fig. S4), nitrogen adsorption/desorption isotherms of HMLC (Fig. S5) and the recent reports about anode materials for SIBs (Table S1) are shown in Supporting Information, which is available from the Nano Energy Library or from the author.

Appendix A. Supporting information

Supplementary data associated with this article can be found in the online version at doi:10.1016/j.nanoen.2018.07.021.

References

[1] J.B. Goodenough, K.S. Park, J. Am. Chem. Soc. 135 (2013) 1167.
[2] D. Kunndu, E. Talaie, V. Duffort, L.F. Nazar, Angew. Chem. Int. Ed. Engl. 54 (2015) 3431–3448.
[3] Y. Sun, J. Tag, K. Zhang, J. Yuan, J. Li, D.-M. Zhu, K. Ozawa, L.-C. Qin, Nanoscale 9 (2017) 2585–2595.
[4] X. Song, X. Li, Z. Bai, B. Yan, D. Li, X. Sun, Nano Energy 26 (2016) 533–540.
[5] H. Liu, H. Guo, B.H. Liu, M.F. Liang, Z.L. Lv, K.R. Adair, X.L. Sun, Adv. Funct. Mater. (2018) 1707480.
[6] S. Wang, L. Xia, L. Yu, L. Zhang, H. Wang, X.W. Lou, Adv. Energy Mater. 6 (2016) 1502217.
[7] M.D. Slater, D. Kim, E. Lee, C.S. Johnson, Adv. Funct. Mater. 23 (2013) 947–958.
[8] K.F. Mak, J. Shan, Nat. Photon 10 (2016) 216–226.
[9] Y. Cai, H. Yang, J. Zhou, Z. Luo, G. Fang, S. Liu, A. Pan, S. Liang, Chem. Eng. J. 327 (2017) 522–529.
[10] W.H. Ryu, H. Wilson, S. Sohn, J. Li, X. Tong, E. Shaulsky, J. Schroers, M. Elimelech, A.D. Taylor, ACS Nano 10 (2016) 3257–3266.
[11] Q. Pang, Y. Gao, Y. Zhao, Y. Ju, H. Qiu, Y. Wei, B. Liu, B. Zou, F. Du, G. Chen, Chemistry 23 (2017) 7074–7080.
[12] H. Zhou, Z.L. Lv, H. Liu, M.F. Liang, B.H. Liu, H. Guo, Electrochim. Acta 250 (2017) 376–383.
[13] S. Deng, Y. Zhong, Y. Zeng, Y. Wang, Z. Yao, F. Yang, S. Lin, X. Wang, X. Lu, X. Xia, J. Tu, Adv. Mater. 29 (2017) 1700748.
[14] W. Sun, P. Li, X. Liu, J. Shi, H. Sun, Z. Tao, F. Li, J. Chen, Nano Res. 10 (2017) 2210–2222.
[15] X. Huang, Z. Zeng, H. Zhang, Chem. Soc. Rev. 42 (2013) 1934–1946.
[16] H. Jiang, D. Ren, H. Wang, Y. Hu, S. Guo, H. Yuan, P. Hu, L. Zhang, C. Li, Adv. Mater. 27 (2015) 3687–3695.
[17] Z. Hu, L. Wang, K. Zhang, J. Wang, F. Cheng, Z. Tao, J. Chen, Angew. Chem. 126 (2014) 13008–13012.
[18] X. Zhang, R. Zhao, Q. Wu, W. Li, C. Shen, L. Ni, H. Yan, G. Diao, M. Chen, ACS Nano 11 (2017) 842.
[19] Y.N. Ko, S.H. Choi, S.B. Park, Y.C. Kang, Nanoscale 6 (2014) 10511–10515.
[20] D. Xie, W. Tang, Y. Wang, X. Xia, Y. Zhong, D. Zhou, D. Wang, X. Wang, J. Tu, Nano Res. 9 (2016) 1618–1629.
[21] H. Wang, X. Wang, L. Wang, J. Wang, D. Jiang, G. Li, Y. Zhang, H. Zhong, Y. Jiang, J. Phys. Chem. C 119 (2015) 10197–10205.
[22] H. Wang, X. Lan, D. Jiang, Y. Zhang, H. Zhong, Z. Zhang, Y. Jiang, J. Power Sources 283 (2015) 187–194.
[23] G.D. Park, J.H. Kim, S.K. Park, Y.C. Kang, ACS Appl. Mater. Interfaces 9 (2017) 10673–10683.
[24] H. Guo, L. Liu, Ti Li, W. Chen, Y. Wang, W. Wang, Chem. Commun. 50 (2014) 673.
[25] Y.J. Hong, M.Y. Son, Y.C. Kang, Adv. Mater. 25 (2013) 2279–2283.
[26] a) H.W. Zhang, L. Zhou, O. Noonan, D.J. Martin, A.K. Whittaker, C.Z. Yu, Adv. Funct. Mater. 24 (2014) 4337–4342;
b) H. Guo, R. Mao, D. Tian, W. Wang, X. Yang, S. Wang, J. Mater. Chem. A 1 (2013) 3652.
[27] L. Yu, B.Y. Guan, W. Xiao, X.W. Lou, Adv. Energy Mater. 5 (2015) 1500981.
[28] H. Guo, L. Liu, T. Li, W. Chen, J. Liu, Y. Guo, Y. Guo, Nanoscale 6 (2014) 5491.
[29] B.J. Guo, Y. Feng, X.F. Chen, B. Li, K. Yu, Appl. Surf. Sci. 434 (2018) 1021–1029.
[30] J.J. Zhang, M.H. Wu, T. Liu, W.P. Kang, J. Xu, J. Mater. Chem. A 5 (2017) 24859–24866.
[31] Y.F. Zhang, A.Q. Pan, L. Ding, Z.L. Zhou, Y.P. Wang, S.Y. Niu, S.Q. Liang, G.Z. Cao,

ACS Appl. Mater. Interfaces 9 (2017) 3624–3633.
[32] F. Niu, J. Yang, N.N. Wang, D.P. Zhang, W.L. Fan, J. Yang, Y.T. Qian, Adv. Funct. Mater. 27 (2017) 1700522.
[33] Y. Tang, Z. Zhao, Y. Wang, Y. Dong, Y. Liu, X. Wang, J. Qiu, ACS Appl. Mater. Interfaces 8 (2016) 32324–32332.
[34] H. Jiang, D. Ren, H. Wang, Y. Hu, S. Guo, H. Yuan, P. Hu, L. Zhang, C. Li, Adv. Mater. 27 (2015) 3687–3695.
[35] M. Minakshi, M.J. Barmi, R.T. Jones, Dalton Trans. 46 (2017) 3588e–3600e.
[36] M.J. Barmi, M. Minakshi, Chempluschem 81 (2016) 964–977.
[37] H. Tang, K. Dou, C. Kaun, Q. Kuang, S. Yang, J. Mater. Chem. A 2 (2014) 360.
[38] D. Xie, W. Tang, Y. Wang, X. Xia, Y. Zhong, D. Zhou, D. Wang, X. Wang, J. Tu, Nano Res. 9 (2016) 1618–1629.
[39] H. Wang, X. Wang, L. Wang, J. Wang, D. Jiang, G. Li, Y. Zhang, H. Zhong, Y. Jiang, J. Phys. Chem. C 119 (2015) 10197–10205.
[40] X. Zhou, L.J. Wan, Y.G. Guo, Chem. Commun. 49 (2013) 1838–1840.
[41] Q. Wang, J. Li, J. Phys. Chem. C 111 (2007) 1675–1682.
[42] Z. Zhang, Y. Fu, X. Yang, Y. Qu, Z. Zhang, Chem. Nano Mater. 1 (2015) 409–414.
[43] Z. Hu, L. Wang, K. Zhang, J. Wang, F. Cheng, Z. Tao, J. Chen, Nano Res. 9 (2016) 1618–1629.
[44] Z.T. Shi, W. Kang, J. Xu, Y.W. Sun, M. Jiang, T.W. Ng, H.T. Xue, D.Y.W. Yu, W. Zhang, C.S. Lee, Nano Energy 22 (2016) 27–37.
[45] K. Zhang, Z. Hu, X. Liu, Z. Tao, J. Chen, Adv. Mater. 27 (2015) 3305–3309.
[46] Y. Jiang, M. Wei, J. Feng, Y. Ma, S. Xiong, Energy Environ. Sci. 9 (2016) 1430–1438.

Hui Liu is pursuing her Master degree at School of Chemical Science and Technology, Yunnan University, China. She received her B.Sc. degree at School of Science, Nanchang University, China. Her research interests are focused on advanced functional materials of lithium-ion batteries, sodium-ion batteries and lithium metal anodes.

Hong Guo is a Professor at Yunnan Key Laboratory of Micro/Nano Materials and Technology, School of Materials Science and Engineering, Yunnan University, China. He received his Ph.D. from University of Science &Technology Beijing in 2008. His research interests are focused on advanced materials for electrochemical energy storage and conversion, including electrode and solid-state electrolyte materials for sodium-ion battery.

Prof. Xueliang Sun is a Canada Research Chair in Development of Nanomaterials for Clean Energy, Fellow of the Royal Society of Canada and Canadian Academy of Engineering and Full Professor at the University of Western Ontario, Canada. Dr. Sun received his Ph.D. in materials chemistry in 1999 from the University of Manchester, UK, which he followed up by working as a postdoctoral fellow at the University of British Columbia, Canada. His current research interests are focused on advanced materials for electrochemical energy storage and conversion, including electrocatalysis in fuel cells and electrodes in lithium-based batteries, metal-air batteries and solid-state batteries.